

DiffFuSR: Super-Resolution of all Sentinel-2 Multispectral Bands using Diffusion Models

Muhammad Sarmad , Michael Kampffmeyer , *Senior Member, IEEE*, and Arnt-Børre Salberg , *Member, IEEE*

Abstract—This paper presents *DiffFuSR*, a modular pipeline for super-resolving all 12 spectral bands of Sentinel-2 Level-2A imagery to a unified ground sampling distance (GSD) of 2.5 meters. The pipeline comprises two stages: (i) a diffusion-based super-resolution (SR) model trained on high-resolution RGB imagery from the NAIP and WorldStrat datasets, harmonized to simulate Sentinel-2 characteristics; and (ii) a learned fusion network that upscales the remaining multispectral bands using the super-resolved RGB image as a spatial prior. We introduce a robust degradation model and contrastive degradation encoder to support blind SR. Extensive evaluations of the proposed SR pipeline on the OpenSR benchmark demonstrate that the proposed method outperforms current SOTA baselines in terms of reflectance fidelity, spectral consistency, spatial alignment, and hallucination suppression. Furthermore, the fusion network significantly outperforms classical pansharpening approaches, enabling accurate enhancement of Sentinel-2's 20 m and 60 m bands. This study underscores the power of harmonized learning with generative priors and fusion strategies to create a modular framework for Sentinel-2 SR. Our code and models can be found at <https://github.com/NorskRegnesentral/DiffFuSR>.

Index Terms—Super-resolution, Sentinel-2, diffusion models, Wald protocol, data fusion

I. INTRODUCTION

THE democratization of Earth observation has been significantly propelled by the advent of open-access satellite missions such as Sentinel-2, which offer freely available multispectral imagery on a global scale. This data serves as a valuable resource for a broad spectrum of applications, including land cover mapping, agricultural monitoring, urban planning, and disaster response [1]. Despite the relatively high spatial resolution of some Sentinel-2 bands (up to 10 m), a substantial portion of the spectral channels, particularly those at 20 m and 60 m, remain too coarse for tasks that demand fine-grained spatial details. This disparity in resolution across bands limits the full exploitation of the data, especially in applications requiring pixel-level precision. There exist several other satellite sensors that provide RGB and multispectral imagery with higher resolution than Sentinel-2, e.g., WorldView 2, 3 and Legion from Maxar, Pléiades from Airbus, and PlanetScope from Planet Labs. However, this data is not freely available, and the acquisition costs may be substantial. Given the global coverage and open availability of Sentinel-2's data, enhancing the spatial resolution through computational means is therefore a highly attractive prospect.

To fully leverage the potential of Sentinel-2's multispectral imagery, super-resolution (SR) has emerged as a compelling approach for enhancing the spatial details [2]–[6]. SR refers to reconstructing high-resolution images from their lower-resolution counterparts, often using data-driven or model-based techniques. Mathematically, SR is regarded as an ill-posed problem as there is a non-uniqueness of the solution. For a given low-resolution (LR) image, there are theoretically an infinite number of high-resolution (HR) images that could have produced that LR image when down-sampled. As the down-sampling process inherently loses high-frequency information (details), reversing this process means trying to infer this lost information, and many different “guesses” can be consistent with the LR input. Moreover, SR is also criticized for its reliance on learned priors and the risk of generating hallucinated details [7]. However, when applied judiciously, with a clear understanding of its limitations, it can significantly improve both the visual interpretability and the utility of satellite imagery in downstream analytical tasks. In the context of Sentinel-2, which consists of multispectral bands in 10 m, 20 m and 60 m resolution, an opportunity arises to combine SR with data fusion techniques to enhance spatial resolution further. Unlike conventional SR, which relies solely on low-resolution inputs, fusion approaches, such as pansharpening, leverage the higher-resolution spectral bands (e.g., the 10 m RGB bands) as guiding information to reconstruct finer details in the lower-resolution bands (e.g., 20 m and 60 m) [8], [9]. This reduces the ambiguity associated with SR by anchoring the reconstruction in real, higher-resolution measurements.

In this work, we propose DiffFuSR, a two-step pipeline that addresses the SR of Sentinel-2 imagery in a comprehensive manner. Our approach begins by super-resolving the 10 m-resolution RGB bands to an enhanced spatial resolution of 2.5 m. Focusing initially on RGB is particularly strategic: the majority of high-resolution reference data available, whether from commercial satellites or aerial imagery, is limited to RGB channels, rather than the full 12-band Sentinel-2 spectrum. Consequently, prioritizing RGB SR allows for effective learning from widely available datasets while remaining consistent with practical downstream applications.

Building upon the super-resolved 2.5 m RGB imagery, we then develop a data fusion strategy to upscale the remaining spectral bands to a unified 2.5 m spatial resolution. For each individual lower-resolution band, the corresponding 2.5 m RGB signal serves as a high-frequency spatial prior, guiding the fusion process. This design allows us to simultaneously preserve the spectral integrity of each band while enriching it with the fine-grained structural information captured in the RGB reference, thus mitigating the risks typically associated

Muhammad Sarmad and Arnt-Børre Salberg are with the Norwegian Computing Center, Oslo, Norway (e-mail: salberg@nr.no).

Michael Kampffmeyer is with the Department of Physics and Technology, UiT The Arctic University of Norway, Tromsø, Norway, and with the Norwegian Computing Center, Oslo, Norway.

with hallucination in purely SR-based approaches.

For the RGB SR step, we develop a diffusion-based model to enhance the spatial resolution of the Sentinel-2 RGB bands to 2.5 m. While diffusion models have gained traction in natural image generation [10]–[12], their application to remote sensing SR remains limited. In addition to diffusion models, we leverage large and diverse training datasets and carefully address domain-specific challenges. We utilize a diverse corpus from aerial NAIP imagery [3] and satellite-based WorldStrat data [13], despite their substantial spectral and radiometric differences from Sentinel-2. To bridge these gaps, we apply spectral harmonization techniques [3], which prove critical for generalization. Additionally, we incorporate blind kernel modeling [14] to simulate unknown degradations typical in real-world Sentinel-2 data. Evaluations using the OpenSR benchmark [15] and qualitative results show that our models yield significant performance improvements over current state-of-the-art baselines [3], [16]–[18].

For enhancing the resolution of the remaining multispectral bands, we design three dedicated fusion pipelines targeting the 10 m, 20 m, and 60 m bands, respectively. Each fusion model leverages the super-resolved 2.5 m RGB imagery as a high-frequency spatial prior, adopting a structure inspired by pansharpening principles. To enable supervised learning without external HR references, we simulate LR training pairs using the Wald protocol [19] on native Sentinel-2 data. The input configuration is tailored to each task: 10 m bands use only native 10 m inputs; 20 m bands combine 10 m and 20 m data; and 60 m bands integrate 10 m, 20 m, and 60 m channels. This targeted design ensures that each fusion task fully exploits the available spatial information. Evaluations show that our learned fusion models significantly outperform classical methods such as Gram-Schmidt pansharpening [20] in terms of quantitative metrics such as ERGAS, PSNR, and SSIM, as well as improved visual fidelity and spectral consistency.

In summary, this work presents a unified framework for super-resolving all Sentinel-2 bands to a common 2.5 m resolution. Unlike previous methods that have addressed either RGB SR or limited multispectral fusion separately, our approach integrates both into a modular, end-to-end pipeline capable of blind SR across all spatial resolutions and spectral channels. The key contributions are summarized as follows:

- A novel diffusion-based SR framework for Sentinel-2 RGB bands, leveraging large-scale aerial and satellite datasets, enhanced with data harmonization and blind kernel modeling to ensure robust generalization across diverse acquisition conditions.
- A new data fusion framework for multispectral super-resolution that enhances the resolution of all Sentinel-2 bands (10 m, 20 m, and 60 m) to a unified 2.5 m spatial resolution using only native Sentinel-2 data, trained using Wald protocol simulations.
- A comprehensive analysis of cross-domain SR challenges, demonstrating the critical importance of harmonization and degradation modeling through rigorous evaluation on the recently proposed OpenSR benchmark.

The rest of the paper is organized as follows: Section II reviews existing SR models, with a focus on Earth observation applications. Section III details the methodologies that constitute the SR pipeline. Section IV describes the experiments and results, focusing on well-known benchmark datasets. The discussion is provided in Section VI, and finally, Section VII concludes this work.

II. BACKGROUND AND RELATED WORKS

Super-resolution (SR) has a rich history, with early breakthroughs focusing on enhancing the resolution by utilizing known relative displacements in image sequences [21], and single image SR using of sparse representations in terms of coupled dictionaries jointly trained from high- and low-resolution image patch pairs [22]. The introduction of deep learning in computer vision was early adapted for SR. Pioneering efforts that demonstrated the potential of convolutional neural network (CNNs) in enhancing image resolution include the SRCNN approach by Dong et al. [23].

Enhancing the resolution of remote sensing images, particularly from satellites, is extremely valuable, as it significantly enhances the utility of the data. Many satellite sensors (e.g., Landsat, WorldView 2 & 3, SPOT 6, ...) have therefore been equipped with a panchromatic band in higher resolution, which offers a more detailed view of features on the ground. Pansharpening, i.e., methods that utilize the panchromatic band to enhance the resolution of simultaneously acquired multispectral data, has consequently been a research topic for decades [24].

However, not all satellite sensors have a panchromatic band; hence, single-image SR has also become a central focus in remote sensing, particularly for enhancing the spatial resolution of Sentinel-2 imagery. Early work, such as Lanaras et al. [8], focused on enhancing the resolution of the RGB bands using CNNs trained with synthetic data. Later methods expanded to multispectral SR through data fusion approaches, combining multiple Sentinel-2 revisits [4] or external high-resolution sources such as PlanetScope [6].

The generative power of generative adversarial networks (GANs) has also been explored for SR. Early works include the SRGAN approach by Ledig et al. [25], which were further enhanced by Wang et al. [26]. The benefit of using generative methods like GANs for SR is the potential of creating photo-realistic images, contrary to non-generative methods, which tend to create too smooth results [25]. After gaining influence in computer vision, GANs were also adopted to enhance the resolution of remote sensing images (see e.g., [27]). Recent advances in generative modeling have motivated the exploration of diffusion models for SR tasks [10], [11]. In the remote sensing domain, Wu et al. [14] applied conditional diffusion models for Sentinel-2 SR, enhancing only the RGB bands by leveraging paired SPOT 6/7 imagery. However, their approach remains constrained to RGB bands, and the reliance on paired HR datasets limits its direct scalability to the full 12-band Sentinel-2 MSI.

Efforts such as the WorldStrat dataset [13] and the OpenSR benchmark [15], have provided valuable resources for training and evaluating remote sensing SR models under real-world

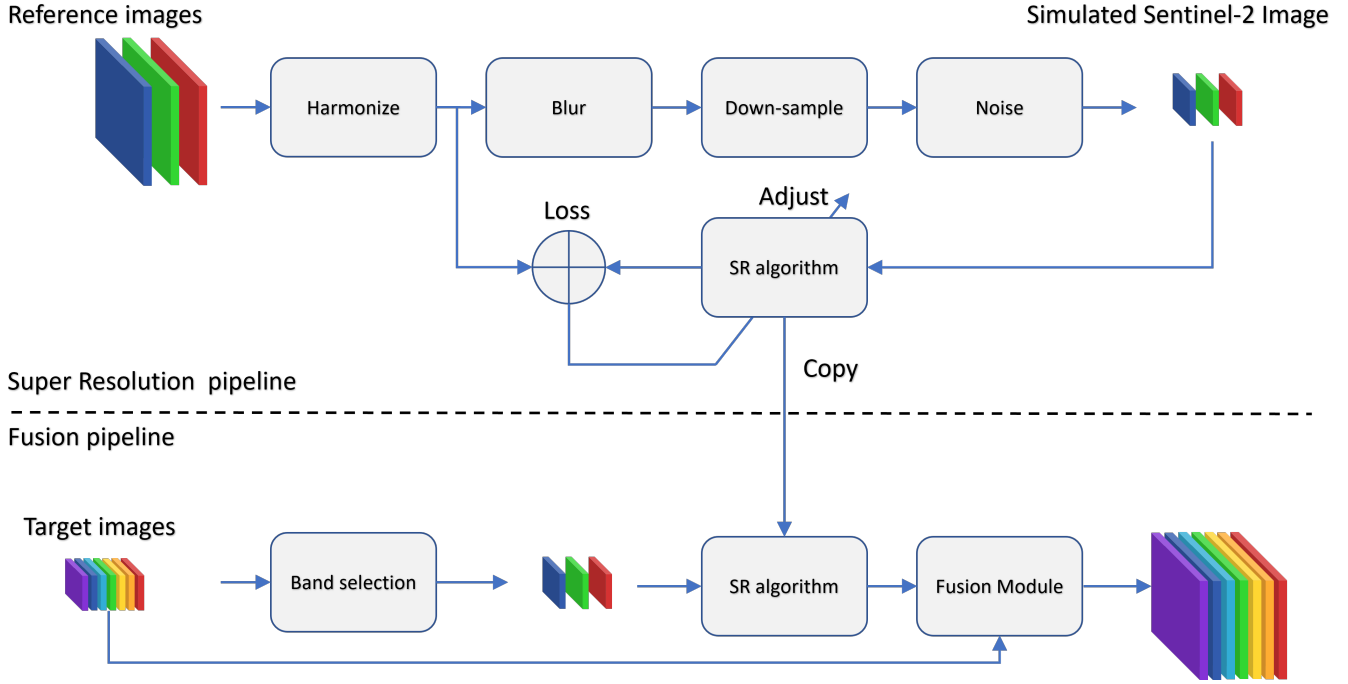


Fig. 1. Overview of the proposed pipeline combining RGB super-resolution and multispectral fusion. The top branch illustrates the training of a denoising diffusion model using synthetic low-resolution RGB images generated through harmonization, blurring, downsampling, and noise addition. The model learns to reconstruct high-resolution RGB images. The bottom branch depicts the fusion process: multispectral Sentinel-2 bands are fused with the super-resolved RGB output via a learned fusion module to produce full-resolution 12-band output.

conditions. Wolters et al. [7] leveraged NAIP aerial imagery for generative SR, but faced challenges due to spectral and radiometric inconsistencies between NAIP and Sentinel-2, leading to domain gaps that degraded the performance. The SEN2NAIP dataset and accompanying work by Aybar et al. [3] introduced a harmonized degradation model to better align NAIP images with Sentinel-2 characteristics, proving crucial for cross-sensor learning. Donike et al. [2] employed latent diffusion models trained on SEN2NAIP, demonstrating that operating in the latent space can significantly reduce resource consumption. They focus solely on super resolving the 10 m Sentinel-2 bands.

Beyond SR, pansharpening techniques have historically been used to fuse high-resolution spatial information with lower-resolution multispectral data [9], [28], [29]. Classical methods such as Gram-Schmidt pansharpening [20] can be effective but may prove insufficient or introduce spectral distortions when attempting to fuse super-resolved RGB images (acting as a pseudo-panchromatic band) with Sentinel-2’s full range of multispectral bands, especially when targeting a significant resolution enhancement to 2.5 m [29]. Lanaras et al. [8] demonstrated that neural networks can perform such fusion more effectively than classical methods, mitigating some distortions. However, their method was limited to enhancing bands to a 10 m ground sampling distance (GSD).

The modular framework presented in this paper significantly extends previous work by jointly addressing super-resolution of all Sentinel-2 bands to a unified 2.5 m resolution. First, we super-resolve the RGB bands using an efficient diffusion model trained on harmonized data, ensuring robust generalization. Second, a dedicated learned fusion network, inspired by pansharpening

principles but trained for superior spectral fidelity, upscales the remaining 10 m, 20 m, and 60 m Sentinel-2 bands. While prior works address isolated components of this problem, to the best of our knowledge, this is the first unified approach that performs blind SR across all Sentinel-2 bands and resolutions.

III. METHOD

The goal of this work is to super-resolve all 12 Sentinel-2 multispectral bands to a unified 2.5 m GSD. First in section III-A, we describe a conditional denoising diffusion model to super-resolve the RGB bands to 2.5 m resolution, trained on harmonized synthetic data to ensure robust generalization. Secondly in section III-B, we introduce a learned multispectral fusion network that leverages the super-resolved RGB output to upscale the remaining Sentinel-2 bands to the target resolution of 2.5 m. The overall pipeline is illustrated in Fig. 1. Next, we will describe each module of the pipeline in detail.

A. Super-Resolution of RGB bands using Conditional Denoising Diffusion Models

We formulate the RGB SR task as conditional generation using a denoising diffusion probabilistic model (DDPM) inspired from [14]. The goal is to generate a HR RGB image $\mathbf{x}_0 \in \mathbb{R}^{C \times H \times W}$, conditioned on a LR observation $\mathbf{x}_{LR} \in \mathbb{R}^{C \times H' \times W'}$, where $H' < H$ and $W' < W$. The model learns to reverse a Gaussian corruption process applied to \mathbf{x}_0 , using the fixed \mathbf{x}_{LR} to create multiple conditioning inputs. The diffusion model based SR pipeline consists of a forward diffusion process and a reverse denoising process (Fig. 2).

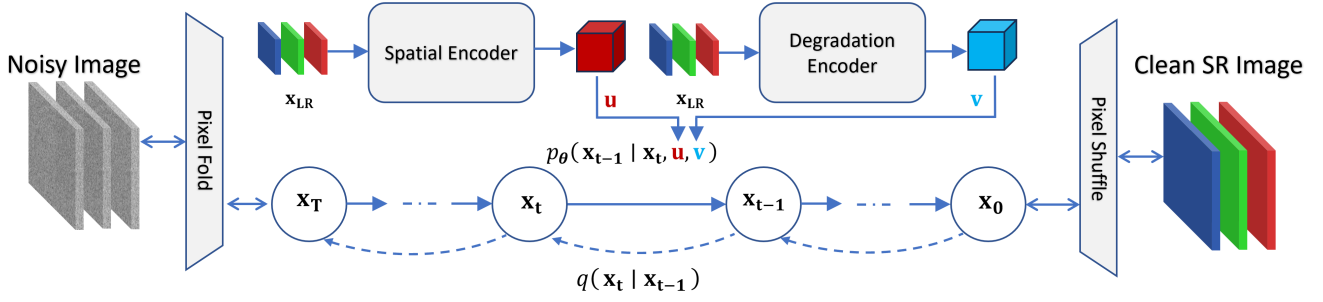


Fig. 2. Architecture of the proposed conditional denoising diffusion model for RGB SR. The model learns to reconstruct a high-resolution RGB image \mathbf{x}_0 from a noisy latent \mathbf{x}_T via a denoising process modeled as a Markov chain. The input image is first degraded with Gaussian noise and spatially rearranged using a pixel-folding operation. A spatial encoder extracts contextual features \mathbf{u} from the low-resolution input, while a degradation encoder produces a global degradation embedding \mathbf{v} . Both \mathbf{u} and \mathbf{v} are used to condition the denoising network at each reverse time step t . The sequence $\mathbf{x}_T \rightarrow \dots \rightarrow \mathbf{x}_0$ is denoised through a learned reverse diffusion process. The final output is reshaped using a pixel shuffle operation to recover the super-resolved RGB image.

1) *Forward Diffusion Process*: Following [30], the forward process is a Markov chain that progressively adds Gaussian noise to a “clean” input image \mathbf{x}_0 over T steps:

$$q(\mathbf{x}_t | \mathbf{x}_{t-1}) = \mathcal{N}(\mathbf{x}_t; \sqrt{\alpha_t} \mathbf{x}_{t-1}, (1 - \alpha_t) \mathbf{I}), \quad (1)$$

with a predefined noise schedule $\{\alpha_t\}_{t=1}^T$. This defines the marginal distribution:

$$q(\mathbf{x}_t | \mathbf{x}_0) = \mathcal{N}(\mathbf{x}_t; \sqrt{\bar{\alpha}_t} \mathbf{x}_0, (1 - \bar{\alpha}_t) \mathbf{I}), \quad (2)$$

where $\bar{\alpha}_t = \prod_{s=1}^t \alpha_s$. At $t = T$, the sample \mathbf{x}_T approximates a standard Gaussian.

2) *Reverse Denoising Process*: The reverse denoising process is modeled as a Markov chain conditioned on the LR input \mathbf{x}_{LR} . This process iteratively denoises a sequence of latent variables $\mathbf{x}_T, \dots, \mathbf{x}_0$ according to:

$$p_\theta(\mathbf{x}_{0:T-1} | \mathbf{x}_T, \mathbf{u}, \mathbf{v}) = \prod_{t=1}^T p_\theta(\mathbf{x}_{t-1} | \mathbf{x}_t, \mathbf{u}, \mathbf{v}), \quad (3)$$

where each reverse transition $p_\theta(\mathbf{x}_{t-1} | \mathbf{x}_t, \mathbf{u}, \mathbf{v})$ is modeled as a Gaussian distribution:

$$p_\theta(\mathbf{x}_{t-1} | \mathbf{x}_t, \mathbf{u}, \mathbf{v}) = \mathcal{N}(\mathbf{x}_{t-1}; \boldsymbol{\mu}_\theta(\mathbf{x}_t, t, \mathbf{u}, \mathbf{v}), \sigma_t^2 \mathbf{I}). \quad (4)$$

The variance σ_t^2 is typically pre-defined, while the mean $\boldsymbol{\mu}_\theta$ is predicted by a denoising network, commonly a U-Net architecture [31], conditioned on the noisy latent \mathbf{x}_t , the timestep t , and the fixed context \mathbf{u}, \mathbf{v} . The conditioning inputs \mathbf{u} and \mathbf{v} are fixed throughout the reverse process and derived from the observed LR image \mathbf{x}_{LR} as follows:

- The spatial feature map $\mathbf{u} = f_\phi(\mathbf{x}_{LR})$ is extracted by an encoder f_ϕ . It captures coarse structural information, such as edges and object geometries from \mathbf{x}_{LR} . The spatial feature map, \mathbf{u} , is concatenated at the input of the UNet.
- The global degradation embedding $\mathbf{v} = g_\psi(\mathbf{x}_{LR})$ summarizes the underlying blur, noise, and downsampling characteristics of \mathbf{x}_{LR} . This embedding is computed using a separate encoder g_ψ , trained via contrastive learning [32], and serves to modulate the denoising network through degradation-aware convolutions. The degradation embedding is injected at multiple positions in the network since it modulates the kernels of degradation-aware convolution layers.

The integration of \mathbf{u} and \mathbf{v} allows the model to incorporate both spatial structural details and degradation-specific behavior, thereby enabling accurate and blind SR.

3) *Network Architecture*: The proposed diffusion model is comprised of three main components (Fig. 2): (i) a *denoising U-Net* that predicts the clean high-resolution image from noisy input, (ii) a *spatial encoder* that extracts contextual features from the low-resolution image, and (iii) a *degradation encoder* trained with contrastive learning to summarize the degradation characteristics. We follow the design by Wu et al. [14].

a) *Denoising U-Net*: The core network h_θ is a conditional U-Net that predicts the clean image \mathbf{x}_0 given a noisy input \mathbf{x}_t , timestep t , and conditioning vectors \mathbf{u}, \mathbf{v} . To improve computational efficiency without losing information, we apply a *pixel folding* operation to \mathbf{x}_t at the input [14]. This reduces spatial resolution by a factor r while increasing the number of channels by r^2 . Formally, this maps an image of dimension $C \times H \times W$ to $(C \cdot r^2) \times (H/r) \times (W/r)$. The inverse of this operation is pixel shuffle as proposed in [33]. We use pixel shuffle to retrieve the full-sized final image. The folded input is passed through the U-Net, which consists of:

- a downsampling path with multiple feature extraction blocks,
- an upsampling path with nearest-neighbour interpolation and convolution, (i.e., spatial resolution is increased by replicating neighboring pixels, followed by refinement with convolution layers)
- residual blocks that incorporate conditioning via timestep embedding and degradation information.

After denoising, the output is unfolded back to the original spatial resolution using the pixel shuffle operation.

To inform the network of the current step in the reverse denoising process, a timestep embedding is injected at each residual block. The scalar timestep $t \in \{1, \dots, T\}$ is first mapped to a sinusoidal positional encoding:

$$\boldsymbol{\kappa}(t) = [\sin(\omega_1 t), \cos(\omega_1 t), \dots, \sin(\omega_d t), \cos(\omega_d t)]^T,$$

and then passed through a multi-layer perceptron (MLP) to produce the embedding \mathbf{t}_e . This embedding is added to intermediate feature maps throughout the U-Net [14].

b) *Spatial Encoder*: The LR input \mathbf{x}_{LR} is processed by a spatial encoder f_ϕ , implemented as an RRDB-Net [26] consisting of 23 Residual-in-Residual Dense Blocks (RRDBs) with 64 feature channels. This architecture is known for its strong performance in SR tasks, particularly its ability to extract hierarchical spatial features without normalization layers. The encoder outputs a spatial feature map $\mathbf{u} = f_\phi(\mathbf{x}_{\text{LR}})$, which serves as a global spatial conditioning signal for the denoising model.

Rather than being fused at multiple layers, the spatial feature map \mathbf{u} is concatenated with the input of the U-Net denoiser at the first layer only. This provides the network with high-level spatial context from the LR image while keeping the fusion interface lightweight. During training, the decoder (a light weight CNN, not shown in Fig. 2) is attached to the encoder to predict a coarse high-resolution reconstruction $\hat{\mathbf{x}}_0$, supervised with an ℓ_1 consistency loss. The decoder is discarded during inference.

c) *Degradation Encoder*: To model the implicit degradation of the LR image, we use a lightweight CNN g_ψ that maps an LR image patch \mathbf{x}_{LR} to a global degradation vector $\mathbf{v} = g_\psi(\mathbf{x}_{\text{LR}})$, following the contrastive learning formulation of [34]. The network consists of several convolutional layers, followed by global average pooling and a projection head. It is trained with a contrastive objective. In the contrastive setting, the goal is to train a model such that given two crops $\mathbf{x}_q, \mathbf{x}_k$ from the same LR image (i.e., with the same degradation), their embeddings $\mathbf{v}_q, \mathbf{v}_k$ should be similar, while embeddings from different images (assumed to have different degradations) should be dissimilar. Under this setting, the model learns about the degradation in an unsupervised manner.

The learned degradation vector \mathbf{v} is injected into each residual block in the U-Net using a degradation-aware convolution (DAConv) layer, as proposed by Wu et al. [14], which adapts the convolutional filters based on the conditioning vector. In this approach, the convolutional filters are dynamically modulated based on the conditioning vector, allowing the network to adapt to different degradation types during inference.

4) *Training Objective*: The model is trained end-to-end using a combination of three loss terms:

- *Denoising loss*: The diffusion model is trained to predict the clean high-resolution image \mathbf{x}_0 from its noisy version \mathbf{x}_t , conditioned on spatial and degradation features using the ELBO loss [30]:

$$\mathcal{L}_{\text{elbo}} = \|\mathbf{x}_0 - h_\theta(\mathbf{x}_t, t, \mathbf{u}, \mathbf{v})\|_1. \quad (5)$$

- *Consistency loss*: An auxiliary decoder, $\xi(\cdot)$, is attached to the spatial encoder f_ϕ , which processes the LR input \mathbf{x}_{LR} . The decoder predicts a coarse HR estimate $\hat{\mathbf{x}}_0 = \xi(f_\phi(\mathbf{x}_{\text{LR}}))$, and the output is compared against the ground truth \mathbf{x}_0 using an L1 loss:

$$\mathcal{L}_{\text{consis}} = \|\hat{\mathbf{x}}_0 - \mathbf{x}_0\|_1. \quad (6)$$

This encourages the spatial encoder to learn features that are aligned with the HR target. The decoder is only used during training and discarded at inference.

- *Contrastive loss*: We use the InfoNCE loss for training. Given two patches \mathbf{x}_{LR} and \mathbf{x}_{LR}^+ from the same image (positive pair), and a set of negatives $\{\mathbf{x}_{\text{LR}}^-\}$ from different images in the batch, the contrastive loss is defined as:

$$\mathcal{L}_{\text{contrast}} = -\log \frac{\exp(\text{sim}(\mathbf{v}, \mathbf{v}^+)/\tau)}{\sum_j \exp(\text{sim}(\mathbf{v}, \mathbf{v}_j)/\tau)}, \quad (7)$$

where $\mathbf{v} = g_\psi(\mathbf{x}_{\text{LR}})$, $\mathbf{v}^+ = g_\psi(\mathbf{x}_{\text{LR}}^+)$, \mathbf{v}_j includes all negative samples, τ is a temperature hyperparameter, and $\text{sim}(\cdot, \cdot)$ denotes cosine similarity, i.e., $\text{sim}(\mathbf{a}, \mathbf{b}) = \frac{\mathbf{a}^T \mathbf{b}}{\|\mathbf{a}\| \|\mathbf{b}\|}$.

The total training loss is then a weighted sum:

$$\mathcal{L}_{\text{total}} = \mathcal{L}_{\text{elbo}} + \mathcal{L}_{\text{consis}} + \lambda_{\text{contrast}} \cdot \mathcal{L}_{\text{contrast}}, \quad (8)$$

where the constant $\lambda_{\text{contrast}}$ is a weighting factor that determines the contribution of the contrastive loss $\mathcal{L}_{\text{contrast}}$ relative to the ELBO loss $\mathcal{L}_{\text{elbo}}$ and the consistency loss $\mathcal{L}_{\text{consis}}$. A small default value, such as $\lambda_{\text{contrast}} = 0.01$, ensures that the contrastive objective improves representation learning without overwhelming the main generative and consistency objectives.

5) *Sampling*: At inference time, a HR image is sampled by starting from $\mathbf{x}_T \sim \mathcal{N}(0, \mathbf{I})$ and iteratively applying the learned denoising model conditioned on \mathbf{u} and \mathbf{v} . The final output \mathbf{x}_0 is returned as the super-resolved RGB image.

Both the spatial encoder f_ϕ and degradation encoder g_ψ receive the same degraded image as input. The randomized degradation ensures that the degradation vector \mathbf{v} is learned from data without relying on ground truth kernels which is key component of the model's blind SR capability. Next, we will describe how we degrade and prepare the HR images for training the diffusion model.

6) *Simulating Sentinel-2 images*: Due to the absence of HR Sentinel-2 imagery suitable for supervised learning, we use HR NAIP aerial images as a proxy to construct synthetic training pairs.

Previous works such as the SEN2NAIP study [3] leverage real, co-registered NAIP–Sentinel-2 pairs to train a harmonization model, comparing a deterministic neural network-based approach with a statistical method grounded in power-law transformations. While the authors did not claim a definitive advantage for either method, they noted that the neural network approach produced slightly sharper visual results for SR. In contrast, we found that learned harmonization does not consistently yield sharper outputs and introduces unnecessary computational overhead. Therefore, we adopt a simpler, statistics-based harmonization model using per-channel power-law transformations.

We generate synthetic LR Sentinel-2-like images by applying a two-stage transformation to NAIP data: (i) spectral harmonization to match Sentinel-2 reflectance distributions, and (ii) randomized degradation to simulate optical and sensor effects such as blur and noise. This strategy enables fully self-supervised training and supports blind SR without reliance on paired ground truth.

a) *Harmonization Model*: Harmonization adjusts the spectral distribution of NAIP imagery to resemble that of Sentinel-2 RGB bands. This process mitigates radiometric discrepancies between the two sensors, enabling more effective cross-domain learning. We perform per-channel gamma correction using a power-law transformation:

$$\hat{\mathbf{x}}_{\text{NP}}^c = \left(\frac{\mathbf{x}_{\text{NP}}^c}{k} \right)^{\frac{1}{\gamma_c}} \cdot k, \quad (9)$$

where \mathbf{x}_{NP}^c denotes band c of the NAIP image, $k = 255$ denotes the dynamic range, and γ_c is the channel-specific gamma value. These gamma values are not arbitrarily chosen; rather, they are derived empirically by aligning NAIP reflectance distributions to co-registered Sentinel-2 imagery. Following the methodology of Aybar et al. [3], optimal gamma values are computed for each channel across a large corpus of image pairs. A multivariate normal model is then fit to the resulting gamma vectors, and the median values are used to define a global correction profile. This ensures consistent spectral alignment during inference without the need for image-specific tuning.

b) Degradation Model: To simulate Sentinel-2-like degradations, we apply a blind degradation strategy that combines randomized blur, downsampling, and additive noise. The degraded image is modeled as:

$$\hat{\mathbf{x}}_{S2} = [\Phi_{\rho}(\hat{\mathbf{x}}_{NP})]_{\downarrow} + \mathbf{n}, \quad (10)$$

where $\Phi_{\rho}(\cdot)$ is a Gaussian blur operator parameterized by ρ , \downarrow denotes bicubic downsampling, and \mathbf{n} is additive Gaussian noise.

c) Blur Model: To emulate optical blur, we use both isotropic and anisotropic Gaussian kernels, with parameters sampled randomly for each training image. We select a fixed kernel size of 21×21 . During training, we use an anisotropic Gaussian blur type, whereas for validation, we use an isotropic Gaussian. We sample the smoothing parameter σ from the range $\sigma \in [2.0, 4.0]$, the eigenvalue range of the anisotropic Gaussian kernel as $\lambda_1, \lambda_2 \in [0.2, 4.0]$, and the rotation angle as $\theta \in [0, \pi]$. Our strategy is different from Aybar et al. [3] since they suggested applying a fixed smoothing parameter (σ) for the blur kernel. From empirical evaluations, we concluded that a blind approach led to better results. In addition, we also found that using both isotropic and anisotropic blur is important.

d) Noise Model: Sensor noise is modeled as additive Gaussian noise, i.e.,

$$\mathbf{n} \sim \mathcal{N}(0, \sigma_n^2 \mathbf{I}), \quad \sigma_n \in [0.0, 25.0], \quad (11)$$

with σ_n sampled randomly for each image during training.

e) Blind Conditioning: The same degraded image is passed to both the spatial encoder f_{ϕ} and the degradation encoder g_{ψ} . The randomized, unsupervised nature of the degradation process enables the model to generalize to unknown test-time corruptions. In particular, the degradation representation \mathbf{v} is learned entirely without supervision of degradation parameters, using contrastive learning to capture differences in blur, noise, and downsampling implicitly.

B. Multispectral Band Fusion

To produce a consistent 2.5 m resolution across all Sentinel-2 bands, we design a learnable fusion approach that reconstructs HR multispectral bands by injecting spatial detail from the super-resolved RGB image (Fig. 3). This is formulated as a guided upsampling problem increasing resolution by pixel replication and feature refinement, where the RGB image provides high-frequency structural cues and the lower-resolution multispectral bands contribute the spectral content.

Let \mathbf{X}_{LR} denote a multispectral data at its native resolution (10 m, 20 m, and 60 m). The objective of the fusion module, $F_v(\cdot, \cdot)$, is to learn a mapping:

$$\hat{\mathbf{X}}_{HR} = F_v(\mathbf{X}_{LR}, \mathbf{x}_0),$$

such that the reconstructed data $\hat{\mathbf{X}}_{HR}$ captures fine structural detail aligned with the super-resolved Sentinel-2 RGB image at 2.5 m GSD from the diffusion module, \mathbf{x}_0 , while remaining spectrally consistent with the original \mathbf{X}_{LR} data. Here \mathbf{v} denotes the parameters of the fusion model. In practice, the fusion pipeline contains three different modules, one for each band group (10m, 20m, 60m), which are trained and tested simultaneously but completely independently of each other, as shown in Fig. 3.

1) Training Strategy and Degradation Simulation: The fusion model is trained in a fully self-supervised manner using only native Sentinel-2 data. No HR targets are assumed. Instead, we adopt a synthetic training strategy: the input bands are downsampled further from their native resolution, and the original band serves as the supervision target. This follows the Wald protocol in spirit, though adapted for groups with no native HR ground truth (e.g., 60 m bands).

To simulate realistic LR observations during training, each input band undergoes a degradation process comprising:

- *Blur:* An optional isotropic Gaussian blur is applied to emulate sensor response.
- *Downsampling:* Spatial resolution is reduced using a *boxcar filter*, implemented as average pooling with stride corresponding to the target scale. This approximates spatial averaging seen in optical sensor acquisition.

At test time, the fusion model receives inputs at the original resolution (10 m, 20 m, or 60 m), along with the super-resolved RGB image in 2.5 m resolution from the diffusion model. The super-resolved RGB input is not used during training. However, the network is expected to learn to generalize zero-shot to enhanced spatial priors from the super-resolved RGB image at 2.5 m [8].

2) Network Implementation: The fusion model $F_v(\cdot, \cdot)$ is instantiated via a separate model for each resolution group (10 m, 20 m, and 60 m), each implemented as a two-branch convolutional network. One branch processes the degraded multispectral inputs, while the other processes a fusion signal derived from auxiliary inputs (e.g., RGB and NIR bands). These branches are merged and refined via a series of residual blocks with dense skip connections.

The inputs to each branch are preprocessed with bilinear interpolation to restore native resolution, after applying blur and boxcar degradation in the training phase. At inference time, the RGB input is substituted with the 2.5 m super-resolved output, allowing the model to exploit high-frequency guidance it has never seen during training.

The model is trained to minimize the ℓ_1 reconstruction loss:

$$\mathcal{L}_{\text{fusion}} = \left\| \hat{\mathbf{X}}_{HR} - \mathbf{X}_{HR} \right\|_1,$$

where \mathbf{X}_{HR} is the native-resolution Sentinel-2 band used as the supervision target, and $\hat{\mathbf{X}}_{HR}$ is the predicted fused output. This objective encourages the model to learn structure-preserving spectral fusion in a purely self-supervised fashion.

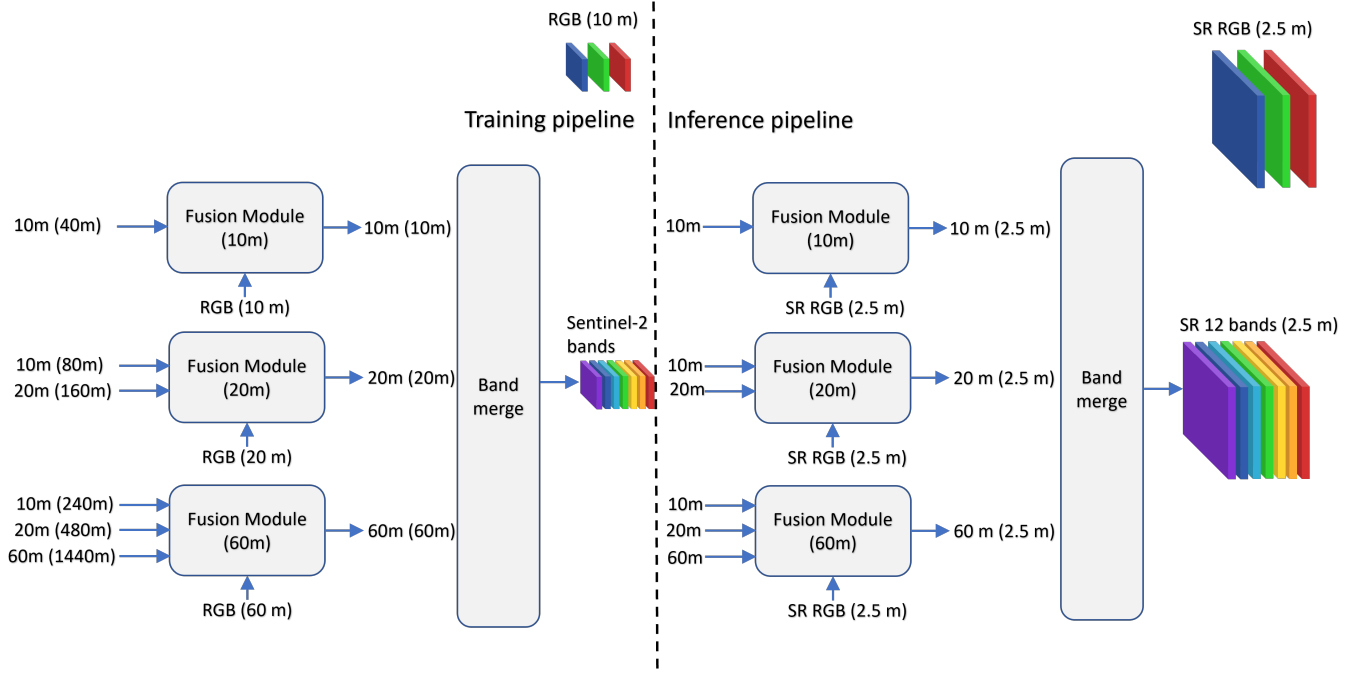


Fig. 3. Architecture of the multispectral fusion pipeline. At test time, each resolution group of 10 m, 20 m, and 60 m bands is processed by a dedicated fusion module that receives the native-resolution multispectral inputs along with the RGB image super-resolved to 2.5 m. These modules independently reconstruct each group at 2.5 m GSD. The outputs are then merged to produce a consistent 12-band super-resolved Sentinel-2 image. This process is applied during both training (using synthetic degraded inputs) and inference (using native-resolution bands), with shared architecture and supervision strategy across all groups. The scaling factor for degraded input for training is computed using the Wald protocol. For example, for the 60 m group, we aim to learn the mapping from 60 m to 2.5 m given a 2.5 m SR guidance signal. This corresponds to a $24\times$ scale factor. During training, all bands (10 m, 20 m, and 60 m) are degraded by this factor, producing input resolutions of 240 m, 480 m, and 1440 m, respectively. At training time, the network reconstructs the degraded signal to 60 m GSD, supervised by the corresponding 60 m ground-truth reference.

IV. EXPERIMENTS AND RESULTS

We will now evaluate the proposed pipeline (DiffFuSR) designed to super-resolve all 12 Sentinel-2 spectral bands to a 2.5-meter GSD. We first describe the datasets utilized for training the diffusion-based SR model and the learned fusion network, followed by their respective training configurations. The performance of DiffFuSR is then benchmarked against established SR and pansharpening baselines. Evaluation is conducted through a comprehensive set of quantitative metrics assessing reflectance accuracy, spectral fidelity, spatial detail, and artifact generation, complemented by qualitative visual comparisons to demonstrate the practical efficacy of the super-resolved products.

A. Datasets

To train and evaluate the proposed SR method, we use the following datasets:

1) *SEN2NAIP Dataset*: The SEN2NAIP dataset [3] consists of two components:

- *Cross-sensor dataset*: Paired imagery from Sentinel-2 and NAIP (National Agriculture Imagery Program), suitable for supervised learning tasks involving cross-sensor translation.
- *Synthetic dataset*: Standalone NAIP images accompanied by transformation parameters for simulating Sentinel-2-like imagery. These parameters are based on four different histogram-based harmonization strategies.

2) *WorldStrat Dataset*: The WorldStrat dataset [13] contains HR RGB imagery acquired from the SPOT satellite. The data is globally distributed and tile-based, covering diverse geographic regions and land cover types. It is designed to support machine learning tasks in remote sensing, such as SR and domain generalization.

3) *Sentinel-2 Data*: The Sentinel-2 data used in this work consists of Level-2A products from the Sentinel-2 mission under the Copernicus program. These products provide 12 spectral bands at spatial resolutions of 10 m, 20 m, and 60 m. All imagery has been curated to be cloud-free and atmospherically corrected, with spatial and temporal alignment across samples. This dataset serves as the LR input for fusion and SR tasks.

B. Training Configurations

We train models using three primary data sources: airborne (NAIP), satellite-based (WorldStrat), and multispectral (Sentinel-2). These datasets are integrated into a unified diffusion-based SR pipeline.

a) *Model Architecture*: The model architecture follows the design of [14] and comprises:

- A degradation encoder for contrastive representation learning.
- A spatial encoder-decoder that is implemented using an RRDB-Net encoder with 23 residual blocks and 64 feature channels.
- A diffusion UNet with 5 residual blocks and channel multipliers $\{1, 2, 2, 4, 8\}$.

- Diffusion configuration: we use 1000 diffusion steps, with a cosine noise schedule following [14]. The model predicts the original clean image \mathbf{x}_0 directly.
- Exponential moving average (EMA) of weights with a decay rate of 0.999.

b) *Training Configuration*: All models were trained for 1000 epochs using the Adam optimizer ($\beta_1 = 0.9$, $\beta_2 = 0.999$) with an initial learning rate of 1×10^{-4} , decayed by a factor of 0.5 at epochs 200, 400, 600, and 800. We used a batch size of 8 and image patch size of 256×256 . Data augmentation included random cropping and flipping.

c) *NAIP (Harmonized and Unharmonized)*: Training used samples from the synthetic set of SEN2NAIP [3]. In the harmonized variant, on-the-fly histogram harmonization was applied during data loading. For unharmonized training, this step was omitted. Both configurations used four-channel multispectral inputs. Degradation modeling applied anisotropic Gaussian blur (kernel size 21, $\sigma \in [2.0, 4.0]$) and additive Gaussian noise with standard deviation 25.

d) *WorldStrat*: A separate model was trained on globally distributed tiles from the WorldStrat dataset [13]. As with NAIP, four-channel input was used and the same model architecture and optimizer configuration were applied. This setup facilitates assessment of generalization across diverse geographies and domains.

C. Fusion Model Training with Sentinel-2

We train a cross-sensor fusion model to enhance spatial resolution in Sentinel-2 multispectral imagery by leveraging HR inputs and multi-resolution contextual information. The fusion model operates over three spatial scales corresponding to Sentinel-2 band groups: 10 m, 20 m, and 60 m resolutions.

a) *Architecture*: The model is a multi-branch variant of RRDB-Net [26], consisting of three dedicated fusion modules:

- A *10 m branch* that fuses RGB and near infrared bands (bands 2, 3 4 and 8).
- A *20 m branch* that fuses the red edge and short wave infrared bands (bands 5, 6, 7, 8A, 11, and 12).
- A *60 m branch* that fuses coastal aerosol and water vapor bands (bands 9 and 10).

Each branch uses an RRDB-Net with 5 residual blocks, 64 base channels, and group convolutions of 32. The fusion signal (i.e., the super-resolved S2 RGB bands) is concatenated with interpolated LR multispectral inputs and used to reconstruct HR outputs at each scale.

The model explicitly accounts for scale differences using a combination of bilinear interpolation, Gaussian blur (pre-smoothing) and boxcar averaging (simulating physical sensor downsampling). These methods are applied dynamically during the forward pass to simulate sensor-specific degradation and harmonize inputs across scales.

b) *Training Details*: Three models are trained using separate optimizers for each spatial branch (10 m, 20 m, 60 m), each using Adam with a learning rate of 1×10^{-4} . A standard L1 loss is applied independently at each scale. Training is conducted in manual optimization mode in PyTorch Lightning, allowing per-branch updates and metric tracking.

c) *Validation Metric*: During validation, the model's outputs are compared to ground truth using the ERGAS metric, computed at each resolution. Additionally, a Gram-Schmidt pansharpening baseline is computed for all outputs.

D. Baseline Methods

Existing state-of-the-art methods do not directly address the task of super-resolving all Sentinel-2 bands to a unified resolution. Since DiffFuSR is modular, we evaluate its components in two stages. First, we compare its RGB SR module against established RGB-specific SR baselines. Second, we evaluate the fusion module separately by comparing it to a suitable multispectral fusion baseline that combines super-resolved RGB with the remaining bands. This decomposition allows for a systematic assessment of each component relative to current state-of-the-art approaches.

1) *Super resolution baselines*: We evaluate our proposed SR approach against a diverse set of existing models, representing a spectrum of training philosophies. The *OpenSR baseline* [3] serves as a strong reference point, particularly due to its use of degradation-based training on NAIP data. The *LDM_Baseline* [18] employs a latent diffusion model, applying generative priors to RGB upsampling, but suffers from instability and hallucination in complex scenes. *Superimage* adopts a pixel-wise regression framework optimized for spectral fidelity. *Satlas* [16], trained using a generative adversarial network [26] on cross-domain imagery, tends to produce sharper images but depicts poor spectral integrity. Additionally, we compare with *SR4RS* [17], a regression-based model targeting RGB SR via auxiliary feature learning, but which introduces spatial inconsistencies in challenging regions.

2) *Fusion model baseline: Gram-Schmidt pansharpening*: To benchmark the effectiveness of the learned fusion network, we implement a classical Gram-Schmidt (GS) pansharpening baseline [9], [28]. This method fuses LR multispectral bands with a HR RGB image, simulating a panchromatic band by averaging the RGB channels. The GS transformation aligns the spectral content of the MS input with the spatial detail of the pan proxy, producing a high-resolution output without learning.

For fair comparison, we apply GS using the same degraded multispectral bands and super-resolved RGB image used by our model at inference time. The GS baseline thus serves as a non-parametric alternative guided by the same spatial prior, highlighting the value added by learned fusion.

E. Metrics

1) *Super Resolution*: We evaluate the proposed SR model using the OpenSR-test benchmark [15], which offers cross-sensor datasets (NAIP, SPOT, Ven μ S, SPAIN CROPS, SPAIN URBAN) with accurately aligned Sentinel-2 LR and HR reference imagery. The benchmark assesses performance through a set of intuitive metrics, grouped into three categories:

Consistency evaluates whether the super-resolved image, when downsampled, preserves key properties of the original Sentinel-2 input. It includes: (i) *reflectance*, measuring radiometric similarity via chosen distance metric; (ii) *spectral*, quantifying preservation of spectral signatures through spectral

angle distance (SAD); and (iii) *spatial*, assessing alignment using phase correlation.

Synthesis captures how much meaningful high-frequency detail the model introduces beyond simple interpolation. Higher synthesis values indicate better recovery of fine structures such as edges, textures, and small objects that are absent in the low-resolution input.

Correctness analyzes whether the generated details are realistic. It includes: (i) *hallucinations*, quantifying spurious details not present in the true HR reference; (ii) *omissions*, measuring genuine high-resolution details that the model failed to recover; and (iii) *improvements*, reflecting correctly added fine-scale structures that were not visible in the low-resolution input. Ideally, hallucination and omission scores should be low, while improvement should be high.

The distance metric chosen for calculation can be either normalized difference distance, LPIPS [35], or CLIP distance [36]. Using all three gives us physical, perceptual, and semantic validation, respectively, which makes OpenSR-test uniquely strong compared to typical SR benchmarks. For full mathematical definitions and implementation details, we refer to the OpenSR-test paper [15].

2) *Fusion Pipeline*: To evaluate the quality of the SR fusion outputs in the absence of ground truth (GT) HR Sentinel-2 imagery, we adopt a no-reference validation strategy. Specifically, we downsample the SR outputs back to the original Sentinel-2 resolution and perform comparisons against the native Sentinel-2 inputs. This indirect supervision enables us to assess fidelity and consistency across multiple quality metrics.

We conduct a quantitative comparison of different fusion methods, neural network (NN) versus GS-based fusion across the 12 Sentinel-2 bands. Evaluations are carried out using the following metrics:

- R^2 : Coefficient of determination, indicating how well predicted reflectance values approximate the actual values. Higher R^2 -values is better, indicating a strong alignment between the predicted and actual values.
- *Cross-Correlation*: Measures the linear relationship between the predicted and original signal. Values close to one indicate strong similarity.
- *SSIM (Structural Similarity Index)*: Assesses perceptual similarity in terms of structure and luminance. Higher values denote more faithful reconstructions [37].
- *PSNR (Peak Signal-to-Noise Ratio)*: Evaluates the ratio between the maximum possible signal and the power of corrupting noise. Higher PSNR suggests better fidelity [37].
- *MSE (Mean Squared Error)*: Captures the average squared difference between the downsampled SR image and the original Sentinel-2 image. Lower values are preferred.
- *ERGAS (Relative Dimensionless Global Error in Synthesis)*: A global error metric specific to remote sensing fusion tasks. Lower values indicate better spectral and spatial consistency [19].

F. Qualitative Evaluation

1) *Super resolution*: Figs. 4 and 5 illustrate qualitative comparisons of the proposed diffusion-based SR model trained

on three different datasets: harmonized NAIP, unharmonized NAIP, and WorldStrat. Each figure is organized into three major rows (one per dataset), where the top row shows reconstructed images, including the LR input, downsampled version, SR output, harmonized SR output, and the HR reference. The second row visualizes per-pixel evaluation maps for reflectance consistency, spectral consistency (SAD), omission space, hallucination space, and improvement space, offering visual insight into the model's behavior.

In Fig. 4, which features a forested scene with green tree cover and bare land, the harmonized NAIP model clearly yields the sharpest and most visually realistic reconstruction. Both the SR image and the harmonized version closely resemble the HR reference, with fine details preserved. This is supported by the quantitative overlays, where reflectance and spectral consistency metrics are lowest (L1: 0.0021, SAD: 1.3884) and omission and hallucination errors are moderate. The unharmonized NAIP variant performs reasonably well but introduces more spectral error and slightly higher hallucination (SAD: 1.5671, HA: 0.4705). The WorldStrat-trained model appears perceptually blurrier and less structurally aligned, despite having similar reflectance L1, and its SAD score (2.10) and omission space distance (0.5530) indicate weaker spectral fidelity. This case highlights the strength of NAIP-derived training, especially in harmonizing the reconstruction of vegetated regions. The likely explanation is that there is a heavy focus on areas with vegetation in NAIP dataset, whereas the WorldStrat dataset has a slight urban area tilt.

Conversely, Fig. 5 presents an urban scene with buildings, where the performance trend shifts. Here, the WorldStrat-trained model produces the most visually convincing output with edges being sharp, and structural details like roof boundaries and roads being clearly resolved. Despite having a slightly higher spectral error (SAD: 1.8039), its visual quality surpasses that of both NAIP-trained models. The harmonized NAIP model underperforms in this case, with noticeable blurring and misalignment around fine structures, and a higher hallucination score (0.4900). This result demonstrates that while NAIP performs well in vegetated regions, it may struggle in built-up areas where WorldStrat's diverse urban coverage offers an advantage.

2) *Fusion module*: Fig. 6 evaluates the proposed learnable fusion model. Here, we only use the harmonised NAIP-based SR model to create the RGB super-resolved image that is further used for fusion. The columns represent the LR input, GS fusion, and our neural network-based fusion, applied to 60 m bands and visualized in natural and false color. Compared to GS, which often distorts the structure and exaggerates spectral contrast, the fusion model output is visually more consistent with the low-resolution signal while enhancing spatial detail. Particularly in the 60 m bands, the fusion model preserves smooth gradients and subtle features that are entirely lost in GS. These results confirm that the learned fusion pipeline generalizes well and substantially outperforms classical pansharpening.

Together, these examples highlight the importance of dataset diversity and the advantage of learning-based fusion. NAIP excels in natural environments, WorldStrat performs better in urban settings, and neural fusion consistently surpasses

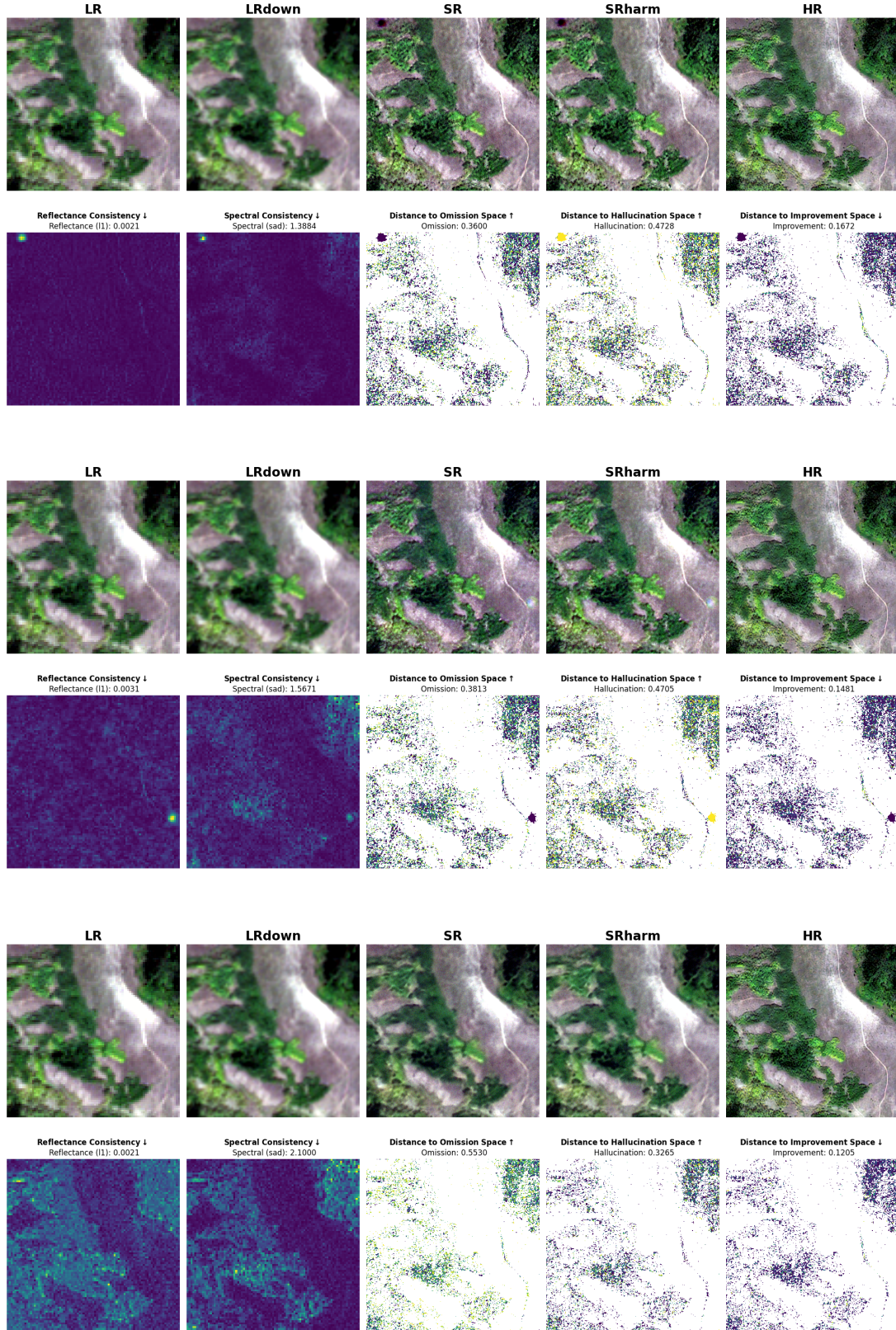


Fig. 4. Qualitative comparison of RGB SR results (vegetated scene). Rows correspond to models trained on harmonized NAIP, unharmonized NAIP, and WorldStrat. Top sub-row shows image outputs: LR input, bicubic downsampled variant, SR result, harmonized SR, and ground truth. Bottom sub-row shows reflectance consistency (L1), spectral consistency (SAD), and distances to omission, hallucination, and improvement spaces. The harmonized NAIP model yields the best visual and quantitative performance in this vegetated context.

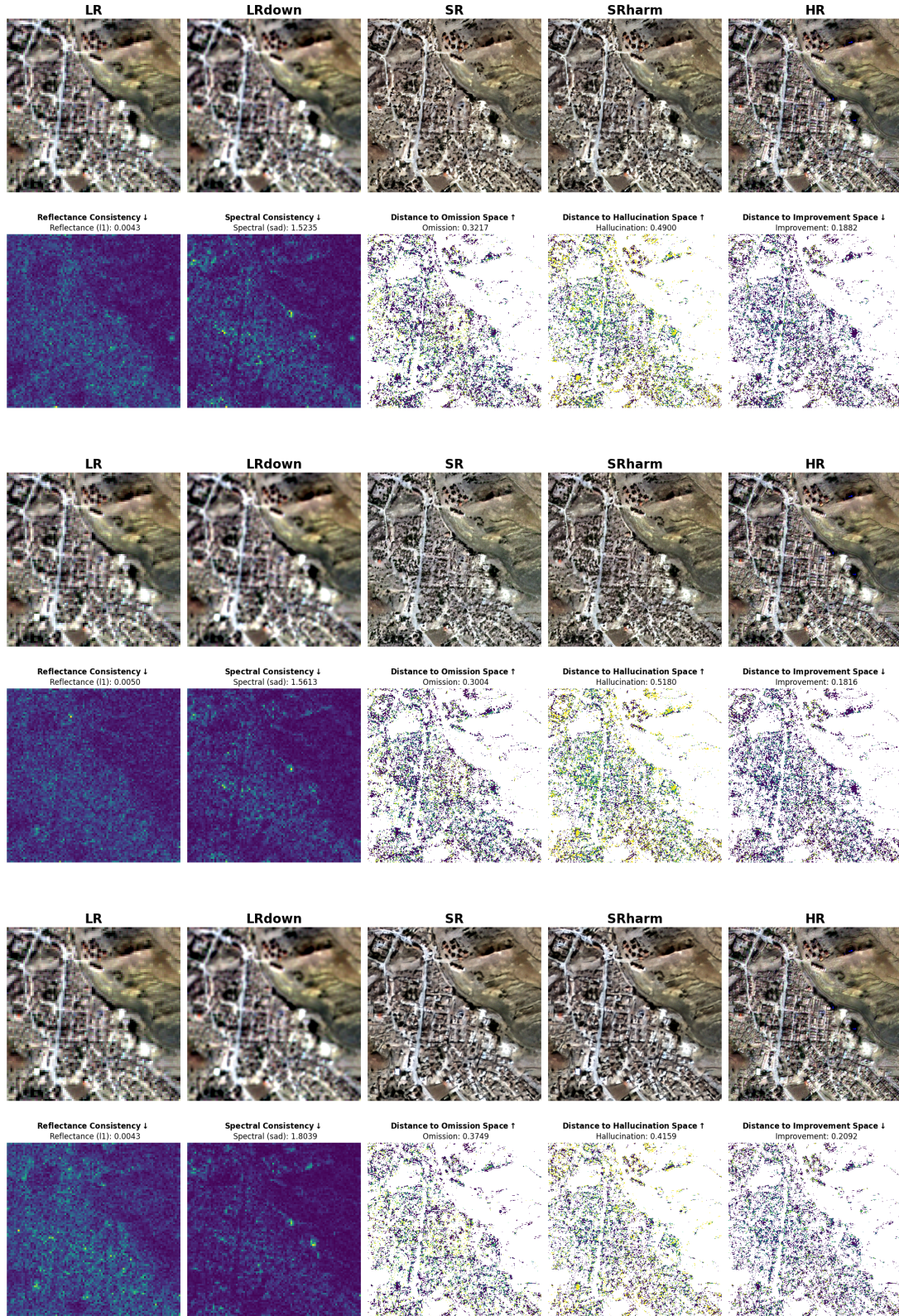


Fig. 5. Qualitative comparison of RGB SR results (urban scene). As in Figure 4, rows represent different training sources. In contrast to the vegetated example, the WorldStrat-trained model produces sharper and more realistic structures in buildings and roads, suggesting stronger generalization in urban domains despite slightly higher spectral error.

TABLE I

NORMALIZED DIFFERENCE-BASED DISTANCE CALCULATION (**BOLD** = BEST, UNDERLINED = SECOND BEST; ↓ LOWER IS BETTER, ↑ HIGHER IS BETTER). “AVG. RANK” SUMMARIZES EACH MODEL’S MEAN RANK ACROSS ALL SEVEN METRICS.

Model	Reflectance ↓	Spectral ↓	Spatial ↓	Synthesis ↑	Hallucination ↓	Omission ↓	Improvement ↑	Avg. Rank
ldm_baseline	0.0505 ± 0.0161	9.6923 ± 2.1742	0.0715 ± 0.0679	0.0285 ± 0.0307	0.6067 ± 0.2172	0.3088 ± 0.1786	0.0845 ± 0.0428	5.57
opensrmodel	0.0031 ± 0.0018	1.2632 ± 0.5878	0.0114 ± 0.0111	0.0068 ± 0.0044	0.3431 ± 0.0738	0.4593 ± 0.0781	0.1976 ± 0.0328	4.00
satlas	0.0489 ± 0.0086	12.1231 ± 3.1529	0.2742 ± 0.0748	<u>0.0227 ± 0.0107</u>	0.8004 ± 0.0641	0.1073 ± 0.0393	0.0923 ± 0.0266	5.71
sr4rs	0.0396 ± 0.0198	3.4044 ± 1.6882	1.0037 ± 0.1520	0.0177 ± 0.0083	0.7274 ± 0.0840	0.1637 ± 0.0572	0.1089 ± 0.0292	5.42
superimage	0.0029 ± 0.0009	1.5672 ± 1.0692	0.0132 ± 0.1131	0.0046 ± 0.0027	0.2026 ± 0.0692	0.6288 ± 0.0754	0.1686 ± 0.0302	5.00
DiffFuSR (NAIP Harm)	0.0024 ± 0.0009	1.1103 ± 0.6197	<u>0.0052 ± 0.0092</u>	0.0083 ± 0.0043	0.4580 ± 0.1020	0.3543 ± 0.0836	<u>0.1876 ± 0.0344</u>	2.85
DiffFuSR (NAIP Unharm)	0.0038 ± 0.0008	<u>1.2320 ± 0.7256</u>	<u>0.0053 ± 0.0093</u>	0.0086 ± 0.0042	0.4927 ± 0.1095	0.3373 ± 0.0870	<u>0.1701 ± 0.0351</u>	3.857
DiffFuSR (Worldstrat)	<u>0.0026 ± 0.0009</u>	1.3277 ± 0.7205	0.0032 ± 0.0074	0.0072 ± 0.0037	0.3915 ± 0.1209	0.4248 ± 0.1058	0.1837 ± 0.0409	<u>3.57</u>

TABLE II

CLIP DISTANCE (**BOLD** = BEST, UNDERLINED = SECOND BEST; ↓ LOWER IS BETTER, ↑ HIGHER IS BETTER). “AVG. RANK” SUMMARIZES EACH MODEL’S MEAN RANK ACROSS ALL SEVEN METRICS.

Model	Reflectance ↓	Spectral ↓	Spatial ↓	Synthesis ↑	Hallucination ↓	Omission ↓	Improvement ↑	Avg. Rank
ldm_baseline	0.1239 ± 0.0405	12.8441 ± 2.7508	0.0717 ± 0.0683	0.0409 ± 0.0290	0.5963 ± 0.3055	0.2327 ± 0.2238	0.1710 ± 0.1435	5.57
opensrmodel	0.0076 ± 0.0046	1.9739 ± 1.0507	0.0118 ± 0.0108	0.0194 ± 0.0120	<u>0.1052 ± 0.0590</u>	0.6927 ± 0.1343	0.2021 ± 0.0854	5.00
satlas	0.1197 ± 0.0233	15.1521 ± 2.9876	0.2766 ± 0.0741	0.0648 ± 0.0302	0.6996 ± 0.2058	0.0872 ± 0.0947	0.2132 ± 0.1393	5.14
sr4rs	0.0979 ± 0.0509	22.4905 ± 2.1168	1.0099 ± 0.0439	<u>0.0509 ± 0.0237</u>	0.3099 ± 0.1704	0.3486 ± 0.1753	0.3415 ± 0.1042	5.28
superimage	0.0068 ± 0.0016	1.8977 ± 1.1053	0.0004 ± 0.0032	0.0130 ± 0.0073	0.0610 ± 0.0305	0.8524 ± 0.0586	0.0866 ± 0.0395	4.28
DiffFuSR (NAIP Harm)	0.0069 ± 0.0032	1.6739 ± 0.8602	0.0061 ± 0.0098	0.0238 ± 0.0120	0.2883 ± 0.2333	0.3358 ± 0.2214	<u>0.3759 ± 0.1444</u>	3.00
DiffFuSR (NAIP Unharm)	0.0109 ± 0.0030	2.0734 ± 1.0205	0.0061 ± 0.0096	0.0245 ± 0.0118	0.3272 ± 0.2400	0.2929 ± 0.2169	0.3799 ± 0.1475	3.92
DiffFuSR (Worldstrat)	0.0075 ± 0.0031	<u>1.7327 ± 0.8545</u>	<u>0.0042 ± 0.0086</u>	0.0205 ± 0.0105	0.2612 ± 0.2544	0.4646 ± 0.2773	0.2742 ± 0.1426	<u>3.71</u>

traditional methods.

G. Quantitative Evaluation

To assess the efficacy of the proposed SR pipeline, we conducted a comprehensive quantitative evaluation across three distance metrics: Normalized Difference, CLIP, and LPIPS [15]. These metrics collectively assess reflectance preservation, spectral and spatial fidelity, and perceptual realism. In addition, we summarize the performance of each method using average rank. To obtain the average rank, each model is ranked individually for every metric: for metrics where lower values indicate better performance (Reflectance, Spectral, Spatial, Hallucination, and Omission), ranks are assigned from lowest (rank 1) to highest (rank 8); for metrics where higher values are better (Synthesis and Improvement), ranks are assigned from highest (rank 1) to lowest (rank 8). The average rank for each model is then computed as the arithmetic mean of its ranks across all seven metrics, providing a single aggregated measure of overall performance.

1) *Performance on Normalized Difference Metrics:* The results in Table I show that the proposed diffusion model, trained on harmonized NAIP data, achieves best-in-class performance in multiple key metrics, including average rank. Specifically, it achieves the lowest reflectance error (0.0024), highest spectral fidelity (1.1103), and the second-best spatial alignment (0.0052). Its synthesis score (0.0083) and omission (0.3543) are high among real competitors, while hallucination errors remain moderate compared to baselines. Notably, our model’s improvement score (0.1876) confirms its strong ability to enrich LR inputs with high-frequency, realistic details.

2) *CLIP Distance Analysis:* Table II further confirms the robustness of DiffFuSR trained with NAIP harmonized data. Reflectance performance is essentially tied with Superimage, and our model delivers the best spectral score (1.6739). Its spatial error (0.0061) is among the lowest, while the improve-

ment metric peaks at 0.3759, indicating an enhanced ability to reconstruct semantically meaningful content.

3) *Insights from LPIPS Metric:* As illustrated in Table III, LPIPS-based analysis shows that the proposed method not only achieves strong perceptual fidelity but also minimizes over-synthesis. It delivers a moderate hallucination score (0.1149), confirming that our model avoids generating too many spurious details. Additionally, it achieves the best improvement score (0.5383), reaffirming its effectiveness in reconstructing rich, high-frequency features from low-resolution imagery.

It is interesting to note that the DiffFuSR-based models achieve the best average ranking across the three Tables.

4) *Fusion-based enhancement of multispectral bands:* To super-resolve all 12 Sentinel-2 bands, we combine RGB upsampling with learned fusion models trained to upscale 10 m, 20 m, and 60 m bands to a unified 2.5 m resolution. Table IV presents a comparison with classical GS pansharpening. Across all data sources, our neural network (NN)-based fusion dramatically outperforms GS in terms of ERGAS, PSNR, and SSIM. For instance, ERGAS drops from over 2900 (GS) to under 95 (NN), PSNR increases from 22 dB to 32 dB, and SSIM rises from 0.65 to 0.88.

V. DISCUSSION

We presented DiffFuSR, a modular pipeline to super-resolve all 12 spectral bands of Sentinel-2 imagery to a 2.5 m GSD, leveraging a diffusion-based model for RGB SR and a learned network for multispectral fusion. The evaluation of the proposed RGB SR model against several contemporary baselines on the OpenSR-test benchmark demonstrated its capabilities in quantitative terms. However, the qualitative results need to be paired with quantitative results to accurately gauge the true performance. Looking at one of the columns of results in quantitative Tables can be misleading, e.g., Satlas and LDM_Baseline seem to be doing the best in terms of Omission

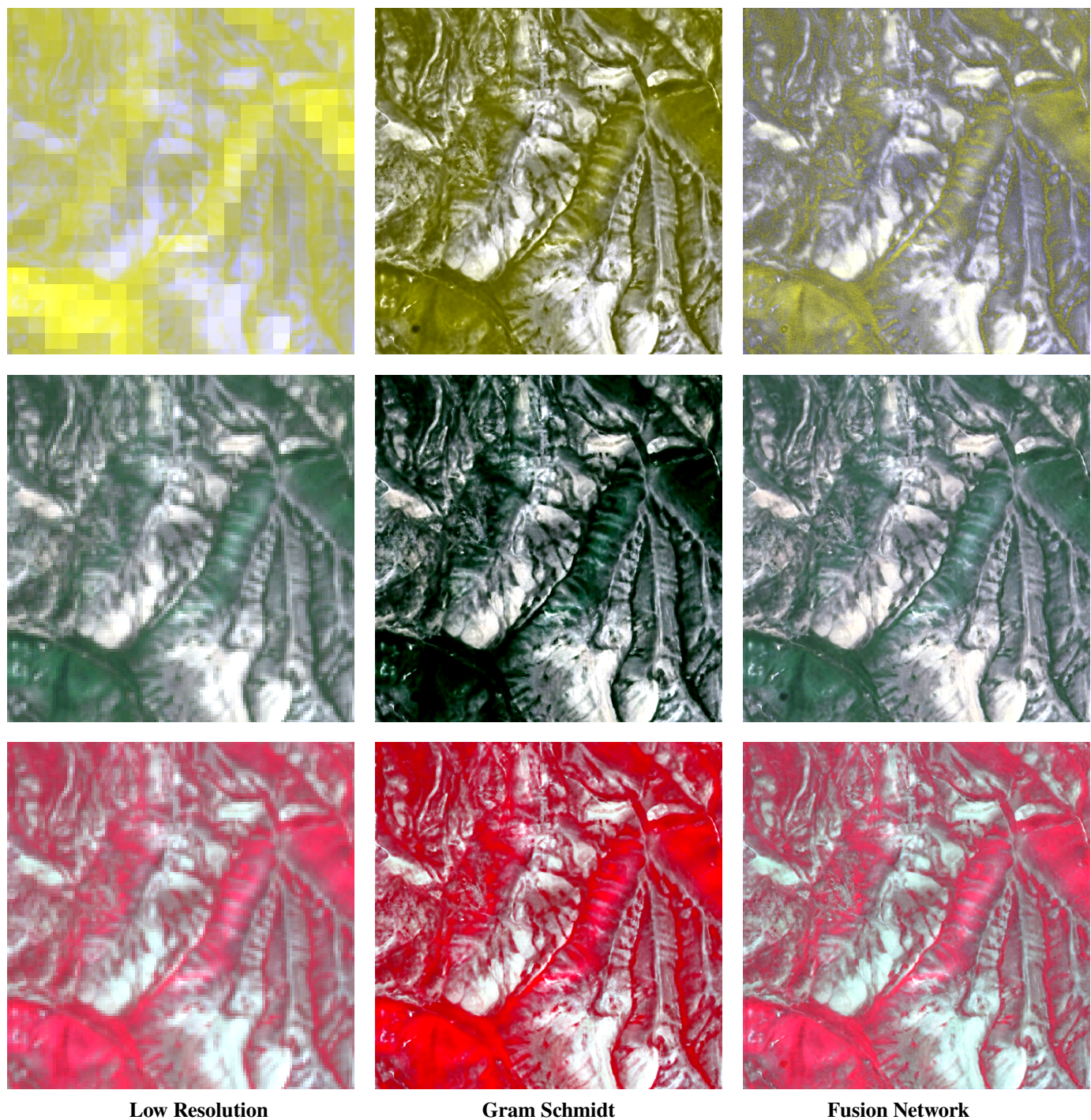


Fig. 6. Fusion output comparisons across 60 m atmospheric bands (top row), natural color (middle), and false color composites (bottom). Each column shows the LR input, GS pansharpening baseline, and our learned neural fusion output. The neural model better preserves semantic structure and avoids the spectral distortions typical in GS fusion, especially in low-texture regions.

TABLE III

LPIPS DISTANCE (**BOLD** = BEST, UNDERLINED = SECOND BEST; ↓ LOWER IS BETTER, ↑ HIGHER IS BETTER). “AVG. RANK” SUMMARIZES EACH MODEL’S MEAN RANK ACROSS ALL SEVEN METRICS.

Model	Reflectance ↓	Spectral ↓	Spatial ↓	Synthesis ↑	Hallucination ↓	Omission ↓	Improvement ↑	Avg. Rank
ldm_baseline	0.1239 ± 0.0405	12.8441 ± 2.7508	0.0717 ± 0.0683	0.0409 ± 0.0290	0.4558 ± 0.2932	0.3558 ± 0.2518	0.1884 ± 0.1232	6.00
opensrmodel	0.0076 ± 0.0046	1.9739 ± 1.0507	0.0118 ± 0.0108	0.0194 ± 0.0120	0.0642 ± 0.0271	0.6690 ± 0.1291	0.2668 ± 0.1071	5.00
satlas	0.1197 ± 0.0233	15.1521 ± 2.9876	0.2766 ± 0.0741	0.0648 ± 0.0302	0.5999 ± 0.2182	0.0588 ± 0.0552	0.3413 ± 0.1858	5.00
sr4rs	0.0979 ± 0.0509	22.4905 ± 2.1168	1.0099 ± 0.0439	0.0509 ± 0.0237	0.3417 ± 0.1833	0.1924 ± 0.1402	0.4659 ± 0.1448	5.00
superimage	0.0068 ± 0.0016	1.8977 ± 1.1053	0.0004 ± 0.0032	0.0130 ± 0.0073	0.0357 ± 0.0200	0.8844 ± 0.0391	0.0800 ± 0.0301	4.28
DiffFuSR (NAIP Harm)	0.0069 ± 0.0031	1.6738 ± 0.8602	0.0060 ± 0.0097	0.0237 ± 0.0120	0.1149 ± 0.1020	0.3466 ± 0.1493	0.5383 ± 0.1240	3.00
DiffFuSR (NAIP Unharm)	0.0109 ± 0.0030	2.0734 ± 1.0205	0.0061 ± 0.0096	0.0245 ± 0.0118	0.1434 ± 0.1158	0.2846 ± 0.1508	0.5720 ± 0.1242	<u>3.85</u>
DiffFuSR (Worldstrat)	0.0075 ± 0.0031	<u>1.7327 ± 0.8545</u>	<u>0.0042 ± 0.0086</u>	0.0205 ± 0.0105	0.0752 ± 0.0682	0.6216 ± 0.1214	0.3032 ± 0.0878	<u>3.85</u>

TABLE IV

QUANTITATIVE COMPARISON OF SUPER-RESOLUTION FUSION METHODS (NN VS. GS) FOR 12 SENTINEL-2 BANDS (BEST ACROSS DATASET IS **BOLD**)

Data Source	Method	R ²	Cross-Correlation	SSIM	PSNR	MSE	ERGAS
NAIP Harmonized	GS	-0.343	0.905	0.648	22.76	1002.61	2972.76
	NN	0.804	0.981	0.877	32.34	143.01	94.83
NAIP Unharmonized	GS	-0.306	0.908	0.656	22.95	977.47	3074.05
	NN	0.805	0.981	0.876	32.10	142.45	95.42
WorldStrat	GS	-0.341	0.905	0.648	22.75	1001.48	57515.33
	NN	0.806	0.981	0.878	32.27	141.96	94.68

metric in Table III. But when looking at the rest of the values and also the qualitative results in Fig. 7, the SR outputs contain severe artefacts.

When trained with harmonized NAIP data, the proposed diffusion model consistently demonstrated superior or highly competitive performance across multiple quantitative metrics, including Normalized Difference, CLIP distance, and LPIPS (Tables I - III). For instance, it achieved the lowest reflectance error (0.0024) and highest spectral fidelity (1.1103) in Normalized Difference metrics, and the best spectral score (1.6739) with CLIP distance. It also recorded a competitive hallucination score (0.1149) using LPIPS, alongside one of the best improvement scores (0.5383) with the same metric, indicating an enhanced ability to reconstruct rich, meaningful high-frequency content with minimal introduction of spurious details. Qualitatively, our model, particularly the harmonized NAIP variant, produced sharper reconstructions with fewer artifacts compared to strong baselines like OpenSR, and markedly better results than LDM_Baseline, Satlas, or Superimage, which exhibited issues such as instability, poor spectral integrity, or over-smoothing, respectively (Fig. 7).

Traditional non-generative SR approaches often optimize for pixel-wise fidelity, which can result in perceptually subdued images. While some modern regression-based models like Superimage offer good reflectance fidelity, our generative approach aims for, and achieves, a compelling balance of perceptual realism and quantitative accuracy. In the domain of generative models, GAN-based approaches like Satlas showed a tendency for poorer spectral integrity despite visual sharpness. Our diffusion model, benefiting from robust training strategies, including the blind degradation modeling, provides a more controlled generation process.

For the subsequent enhancement of all 12 Sentinel-2 bands, the learned multispectral fusion network was evaluated against classical GS pansharpening. The results were definitive: the neural network (NN)-based fusion outperformed GS across all considered metrics (R², Cross-Correlation, SSIM, PSNR,

MSE, and ERGAS) and for all RGB SR inputs (Tab. IV). For example, when using the harmonized NAIP SR RGB, ERGAS values dropped from over 2900 for GS to under 95 for our NN approach, and PSNR increased from approximately 22 dB to over 32 dB. Qualitative comparisons (Fig. 6) further confirmed that our fusion model better preserves semantic structures and avoids the spectral distortions common in GS fusion, especially for the 20 m and 60 m bands.

A critical factor in the success of the RGB SR stage was the spectral harmonization and degradation modeling applied to the proxy HR datasets (NAIP and WorldStrat) to simulate Sentinel-2 characteristics. The superior performance of models trained on harmonized NAIP data, particularly for vegetated scenes (Fig. 4), underscores the importance of these pre-processing steps. The blind degradation modeling, facilitated by a contrastive degradation encoder, is a significant contribution, enabling the SR model to adapt to unseen degradation conditions in real Sentinel-2 imagery without explicit kernel information.

The choice of HR training data also influenced performance, with NAIP-trained models excelling in natural, vegetated environments, while WorldStrat-trained models demonstrated an advantage in structured, urban settings (Figs. 4 and 5). This suggests that while harmonization is effective, the inherent spatial and radiometric properties of the proxy data can still subtly influence model specialization, highlighting the value of diverse training datasets for developing globally applicable models.

The effect of harmonization on NAIP data is most prominent on reflectance and spectral metrics. Other metrics are not affected to the same extent. This is in accordance to our expectation as harmonization brings the spectral content of NAIP closer to Sentinel-2. It is also interesting to note that metrics like hallucination are also slightly reduced, giving interesting insight into the effect of harmonization. On the other hand, the omission metric is actually better in the unharmonized case. This behavior is interesting because it indicates that the SR images have missing details that were present in the HR image.



Fig. 7. Visual comparison of SR methods on OpenSR-test [15] test image. The top row highlights the strongest models: HR reference, our model trained on harmonized NAIP, and OpenSR. The bottom row shows the input LR image and remaining baselines. Among all methods, DiffFuSR produces the sharpest reconstruction with fewer artifacts, while OpenSR is a strong baseline. LDM_Baseline and Satlas produce visibly degraded outputs, and SuperImage tends to oversmooth fine structures.

The learned fusion network, trained using only native Sentinel-2 data via a Wald protocol simulation, proved highly effective. Its ability to utilize the 2.5 m super-resolved RGB output from the diffusion model and to upscale the 10 m, 20 m, and 60 m bands while preserving spectral integrity is a core achievement. The scale-aware design, with dedicated fusion modules and tailored inputs for each Sentinel-2 resolution group (10 m, 20 m, 60 m bands), contributes to the robustness and high fidelity of the final super-resolved Sentinel-2 12-band product. This modularity, both within the fusion stage and in the overall two-stage pipeline, offers practical benefits for future refinement and adaptation. There is room for improvement in the design choices in the Fusion module architecture, which we leave for future work.

VI. CONCLUSIONS

In this work, we proposed and demonstrated DiffFuSR, a pipeline to super-resolve all 12 bands of Sentinel-2. The main contribution of the work was the combination of strengths of both classical and state-of-the-art deep learning methods, and ensuring best practices for pre-processing and harmonizing the data. The work has demonstrated that learning state-of-the-art Sentinel-2 SR models from other data modalities, e.g., NAIP, is not only possible but one of the best ways due to the lack of

paired data. Converting the NAIP data to look like Sentinel-2 is the most critical factor in the pipeline. Small details like the correct kernel size and the type of blur kernel are crucial factors for an accurate degradation model to simulate Sentinel-2 images. By learning from NAIP data with the correct degradation model, we were able to train a diffusion model to super-resolve the RGB bands of Sentinel-2. To super-resolve all 12 bands, the super-resolved RGB image was used to guide the enhancement of the remaining bands in the proposed fusion module.

However, some limitations and areas for future development should be acknowledged. The computational requirements for training and, more critically, for inference with diffusion models are substantial due to their iterative sampling nature. For widespread operational adoption, research into model compression, knowledge distillation, or more efficient sampling strategies specifically for SR tasks will be crucial. While the training datasets (SEN2NAIP, WorldStrat) are extensive, developing models that exhibit even greater robustness across the full diversity of global landscapes and atmospheric conditions will likely benefit from even larger and more varied training corpora, potentially incorporating advanced data augmentation or domain generalization techniques. The reliance on proxy data, even with careful harmonization, may also leave residual domain gap effects that warrant continued research into cross-domain

adaptation.

Future work could extend this framework to incorporate temporal information from Sentinel-2 time series, potentially improving SR quality and enabling consistent 2.5 m analysis-ready data stacks. Adapting the degradation models and fusion strategies for other multispectral satellite sensors could broaden the applicability of this promising pipeline architecture.

ACKNOWLEDGMENTS

Thanks to the European Space Agency, PRODEX program, for funding under the project 4000141281.

REFERENCES

- [1] P. Kansakar and F. Hossain, "A review of applications of satellite earth observation data for global societal benefit and stewardship of planet earth," *Space Policy*, vol. 36, pp. 46–54, 2016.
- [2] S. Donike, C. Aybar, L. Gómez-Chova, and F. Kalaitzis, "Trustworthy super-resolution of multispectral sentinel-2 imagery with latent diffusion," *IEEE J. Sel. Topics Appl. Earth Observ. Remote Sens.*, 2025.
- [3] C. Aybar, D. Montero, J. Contreras, S. Donike, F. Kalaitzis, and L. Gómez-Chova, "Sen2naip: A large-scale dataset for sentinel-2 image super-resolution," *Scientific Data*, vol. 11, no. 1, p. 1389, 2024.
- [4] T. Tarasiewicz, J. Nalepa, R. A. Farrugia, G. Valentino, M. Chen, J. A. Briffa, and M. Kawulok, "Multitemporal and multispectral data fusion for super-resolution of sentinel-2 images," *IEEE Trans. Geosci. Remote Sens.*, vol. 61, pp. 1–19, 2023.
- [5] P. Kowalczyk, T. Tarasiewicz, M. Ziąja, D. Kostrzewa, J. Nalepa, P. Rokita, and M. Kawulok, "A real-world benchmark for sentinel-2 multi-image super-resolution," *Scientific Data*, vol. 10, no. 1, p. 644, 2023.
- [6] N. Latte and P. Lejeune, "Planetscope radiometric normalization and sentinel-2 super-resolution (2.5 m): A straightforward spectral-spatial fusion of multi-satellite multi-sensor images using residual convolutional neural networks," *Remote Sensing*, vol. 12, no. 15, 2020. [Online]. Available: <https://www.mdpi.com/2072-4292/12/15/2366>
- [7] P. Wolters, F. Bastani, and A. Kembhavi, "Zooming out on zooming in: Advancing super-resolution for remote sensing," 2023. [Online]. Available: <https://arxiv.org/abs/2311.18082>
- [8] C. Lanaras, J. Bioucas-Dias, S. Galliani, E. Baltsavias, and K. Schindler, "Super-resolution of sentinel-2 images: Learning a globally applicable deep neural network," *ISPRS J. Photogramm. Remote Sensing*, vol. 146, pp. 305–319, 2018.
- [9] G. Vivone, L. Alparone, J. Chanussot, M. Dalla Mura, A. Garzelli, G. A. Licciardi, R. Restaino, and L. Wald, "A critical comparison among pansharpening algorithms," *IEEE Trans. Geosci. Remote Sens.*, vol. 53, no. 5, pp. 2565–2586, 2014.
- [10] R. Rombach, A. Blattmann, D. Lorenz, P. Esser, and B. Ommer, "High-resolution image synthesis with latent diffusion models," in *Proc. IEEE Conf. Comput. Vis. Pattern Recognit. (CVPR)*, 2022, pp. 10 684–10 695.
- [11] C. Saharia, J. Ho, W. Chan, T. Salimans, D. J. Fleet, and M. Norouzi, "Image super-resolution via iterative refinement," *IEEE Trans. Pattern Anal. Mach. Intell.*, vol. 45, no. 4, pp. 4713–4726, 2022.
- [12] J. Teng, W. Zheng, M. Ding, W. Hong, J. Wangni, Z. Yang, and J. Tang, "Relay diffusion: Unifying diffusion process across resolutions for image synthesis," 2023.
- [13] J. Cornebise, I. Oršolić, and F. Kalaitzis, "Open high-resolution satellite imagery: The worldstrat dataset—with application to super-resolution," *Adv. Neural Inform. Process. Syst.*, vol. 35, pp. 25 979–25 991, 2022.
- [14] H. Wu, N. Ni, S. Wang, and L. Zhang, "Conditional stochastic normalizing flows for blind super-resolution of remote sensing images," *IEEE Trans. Geosci. Remote Sens.*, vol. 61, 2023.
- [15] C. Aybar, D. Montero, S. Donike, F. Kalaitzis, and L. Gómez-Chova, "A comprehensive benchmark for optical remote sensing image super-resolution," *IEEE Geosci. Remote Sens. Lett.*, vol. 21, pp. 1–5, 2024.
- [16] P. Wolters, F. Bastani, and A. Kembhavi, "Zooming out on zooming in: Advancing super-resolution for remote sensing," *arXiv preprint arXiv:2311.18082*, 2023.
- [17] R. Cresson, "SR4RS: A tool for super resolution of remote sensing images," *J. Open Res. Softw.*, vol. 10, no. 1, 2022.
- [18] S. Donike, C. Aybar, L. Gómez-Chova, and F. Kalaitzis, "Trustworthy super-resolution of multispectral sentinel-2 imagery with latent diffusion," *IEEE J. Sel. Topics Appl. Earth Observ. Remote Sens.*, vol. 18, pp. 6940–6952, 2025.
- [19] L. Wald, *Data fusion: definitions and architectures: fusion of images of different spatial resolutions*. Presses des MINES, 2002.
- [20] M. Dalla Mura, G. Vivone, R. Restaino, P. Addesso, and J. Chanussot, "Global and local gram-schmidt methods for hyperspectral pansharpening," in *Proc. IEEE Int. Geosci. Remote Sens. Symp. (IGARSS)*. IEEE, 2015, pp. 37–40.
- [21] M. Irani and S. Peleg, "Improving resolution by image registration," *CVGIP: Graphical Models Image Process.*, vol. 53, no. 3, pp. 231–239, 1991.
- [22] J. Yang, J. Wright, T. S. Huang, and Y. Ma, "Image super-resolution via sparse representation," *IEEE Trans. Image Process.*, vol. 19, no. 11, pp. 2861–2873, 2010.
- [23] C. Dong, C. C. Loy, K. He, and X. Tang, "Image super-resolution using deep convolutional networks," *IEEE Trans. Pattern Anal. Machine Intell.*, vol. 38, no. 2, pp. 295–307, 2015.
- [24] L.-J. Deng, G. Vivone, M. E. Paoletti, G. Scarpa, J. He, Y. Zhang, J. Chanussot, and A. Plaza, "Machine learning in pansharpening: A benchmark, from shallow to deep networks," *IEEE Geosci. Remote Sens. Mag.*, vol. 10, no. 3, pp. 279–315, 2022.
- [25] C. Ledig, L. Theis, F. Huszár, J. Caballero, A. Cunningham, A. Acosta, A. Aitken, A. Tejani, J. Totz, Z. Wang *et al.*, "Photo-realistic single image super-resolution using a generative adversarial network," in *Proc. IEEE Conf. Comput. Vis. Pattern Recognit. (CVPR)*, 2017, pp. 4681–4690.
- [26] X. Wang, K. Yu, S. Wu, J. Gu, Y. Liu, C. Dong, Y. Qiao, and C. Change Loy, "ESRGAN: Enhanced super-resolution generative adversarial networks," in *Proc. Eur. Conf. Comput. Vis. Workshops (ECCVW)*, 2018, pp. 0–0.
- [27] W. Ma, Z. Pan, J. Guo, and B. Lei, "Super-resolution of remote sensing images based on transferred generative adversarial network," in *Proc. IEEE Int. Geosci. Remote Sens. Symp. (IGARSS)*. IEEE, 2018, pp. 1148–1151.
- [28] L. Loncan, L. B. De Almeida, J. M. Bioucas-Dias, X. Briottet, J. Chanussot, N. Dobigeon, S. Fabre, W. Liao, G. A. Licciardi, M. Simoes *et al.*, "Hyperspectral pansharpening: A review," *IEEE Geosci. Remote Sens. Mag.*, vol. 3, no. 3, pp. 27–46, 2015.
- [29] M. Sarmad, M. C. Kampffmeyer, and A.-B. Salberg, "Diffusion models with cross-modal data for super-resolution of sentinel-2 to 2.5 meter resolution," in *IGARSS 2024-2024 IEEE International Geoscience and Remote Sensing Symposium*. IEEE, 2024, pp. 1103–1107.
- [30] J. Ho, A. Jain, and P. Abbeel, "Denoising diffusion probabilistic models," *Adv. Neural Inf. Process. Syst.*, vol. 33, pp. 6840–6851, 2020.
- [31] O. Ronneberger, P. Fischer, and T. Brox, "U-Net: Convolutional networks for biomedical image segmentation," in *Proc. Int. Conf. Med. Image Comput. Comput.-Assist. Interv. (MICCAI)*, Munich, Germany. Springer, 2015, pp. 234–241.
- [32] K. He, H. Fan, Y. Wu, S. Xie, and R. Girshick, "Momentum contrast for unsupervised visual representation learning," in *Proc. IEEE Conf. Comput. Vis. Pattern Recognit. (CVPR)*, 2020, pp. 9729–9738.
- [33] W. Shi, J. Caballero, F. Huszár, J. Totz, A. P. Aitken, R. Bishop, D. Rueckert, and Z. Wang, "Real-time single image and video super-resolution using an efficient sub-pixel convolutional neural network," in *Proc. IEEE Conf. Comput. Vis. Pattern Recognit. (CVPR)*, 2016, pp. 1874–1883.
- [34] L. Wang, Y. Wang, X. Dong, Q. Xu, J. Yang, W. An, and Y. Guo, "Unsupervised degradation representation learning for blind super-resolution," in *Proc. IEEE/CVF Conf. Comput. Vis. Pattern Recognit. (CVPR)*, 2021, pp. 10 581–10 590.
- [35] R. Zhang, P. Isola, A. A. Efros, E. Shechtman, and O. Wang, "The unreasonable effectiveness of deep features as a perceptual metric," in *Proc. IEEE Conf. Comput. Vis. Pattern Recognit. (CVPR)*, 2018, pp. 586–595.
- [36] A. Radford, J. W. Kim, C. Hallacy, A. Ramesh, G. Goh, S. Agarwal, G. Sastry, A. Askell, P. Mishkin, J. Clark *et al.*, "Learning transferable visual models from natural language supervision," in *International conference on machine learning*. PMLR, 2021, pp. 8748–8763.
- [37] Y. Blau and T. Michaeli, "The perception-distortion tradeoff," in *Proceedings of the IEEE conference on computer vision and pattern recognition*, 2018, pp. 6228–6237.